Multistage development of anisotropic magnetic correlations in the Co-based honeycomb lattice $Na_2Co_2TeO_6$

C. H. Lee,[1] S. Lee,[1] Y. S. Choi,[1] Z. H. Jang,[2] R. Kalaivanan,[3] R. Sankar,[3,*] and K.-Y. Choi[4,†]

[1]*Department of Physics, Chung-Ang University, 84 Heukseok-ro, Seoul 06974, Republic of Korea*

[2]*Department of Physics, Kookmin University, Seoul 136-702, Republic of Korea*

[3]*Institute of Physics, Academia Sinica, Taipei 11529, Taiwan*

[4]*Department of Physics, Sungkyunkwan University, Suwon 16419, Republic of Korea*

(Received 16 January 2021; accepted 17 June 2021; published 28 June 2021)

We investigate the thermal evolution of magnetic correlations of the Co-based honeycomb lattice $Na_2Co_2TeO_6$ with ^{23}Na nuclear magnetic resonance and static magnetic susceptibility $\chi(T)$. The studied compound shows three-dimensional (3D) long-range magnetic ordering at $T_N = 26$ K. On cooling through $T^* \approx 110$ K, a simple paramagnetic state undergoes a crossover to a correlated paramagnetic state featuring a power-law dependence of the nuclear spin-lattice ($1/T_1$) and spin-spin ($1/T_2$) relaxation rates as well as of the out-of-plane $\chi(T)$. The magnetic-field-direction dependence of $1/T_1$, $1/T_2$, and $\chi(T)$ uncovers anisotropic spin-spin correlations of a two-dimensional (2D) renormalized classical character. In a magnetically ordered state, we are able to identify four successive transitions or crossovers occurring at $T_N = 26$, $T_{N1} = 16$, $T_{N2} = 7$, and $T_{N3} = 3.5$ K. The multiple transitions and crossovers are associated with the coexistence of 2D and 3D magnetic orders or reorientation of the ordered spins. Our results suggest the presence of various types of frustrating interactions and their energy hierarchy that control complex magnetic structures and anisotropic magnetism.

DOI: 10.1103/PhysRevB.103.214447

I. INTRODUCTION

Since the seminal paper by Kitaev in 2006 [1], impressive progress has been made in realizing a Kitaev spin liquid (KSL) on the bond-dependent honeycomb lattice [2–4]. Most significantly, the Kitaev honeycomb model harbors Majorana fermions that hold promise for the implementation of a fault-free quantum computer.

Following the guiding principle proposed by Jackeli and Khaliullin in 2009 [5], a KSL phase has been sought after in low-spin (LS) d^5 transition metal ions with strong spin-orbit coupling and a $j_{\text{eff}} = 1/2$ Kramers doublet. To date, a handful of KSL materials have been discovered, including A_2IrO_3 (A = Na, Li) and α-$RuCl_3$ [2,4,6–8]. Extensive theoretical and experimental studies have revealed that all the candidate materials reported thus far possess ferromagnetic (FM) Kitaev interactions and entail various perturbation terms detrimental to a KSL phase. To enable the exploration of rich Kitaev physics in a wide parameter range, the original Jackeli and Khaliullin mechanism has been recently extended to a high-spin (HS) d^7 electron configuration [9–12].

Similar to the LS d^5 case, the HS d^7 ($t_{2g}^5 e_g^2$) electron configuration permits exchange processes engendering FM Kitaev interaction. The distinct feature of the HS d^7 magnetism lies in the fact that additional exchange processes can occur through the spin-active e_g electrons, providing channels to nullify Heisenberg-type interactions. From a materials viewpoint, Co^{2+}-based honeycomb compounds having the edge-sharing network of CoO_6 octahedra fulfill the prerequisites for the HS d^7 magnetism. Prominent examples include $Na_2Co_2TeO_6$, $(Na,Li)_3Co_2SbO_6$, and $BaCo_2(AsO_4)_2$ [13–18]. These layered cobaltates constitute a nearly regular octahedron with small trigonal distortions and form a $j_{\text{eff}} = 1/2$ Kramers doublet ground state.

Hereafter, we focus on $Na_2Co_2TeO_6$ (hexagonal space group $P6_322$), which is nearly free from monoclinic distortions. The Co^{2+} honeycomb layers are separated by Na^+ layers, while the TeO_6 octahedra are located at the center of the honeycomb lattice (see Fig. 1). Powder neutron-diffraction and theoretical studies showed the occurrence of long-range zigzag antiferromagnetic (AFM) order at $T_N \approx 27$ K with propagation vector (1/2, 0, 0) [19–21]. Subsequent resonant x-ray diffraction on single crystals uncovered extra anomalies in addition to the 3D AFM order: a two-dimensional (2D) magnetic order at $T_{2D} \approx 31$ K and a small change in the magnetic structure at about 18 K [22]. Moreover, the previously accepted zigzag order at T_N is revised as a triple-**q** order. The magnetic susceptibility below T_N shows even richer magnetic anomalies at $T_{N1} = 16$–17 K and $T_{N3} = 4$ K [19,20,23].

Strikingly, $Na_2Co_2TeO_6$ and α-$RuCl_3$ share many similarities concerning strong magnetic anisotropies between the in-plane and the out-of-plane directions and a field-temperature phase diagram, indicative of the dominance of anisotropic exchange interactions [24]. Recent inelastic neutron scattering measurements purport that the effective spin Hamiltonian of $Na_2Co_2TeO_6$ can be captured within a generalized Kitaev model, although the magnitude of magnetic parameters and the sign of Kitaev interaction are uncertain [25–27]. Magnons in the ordered state defy their description within the zigzag order [22]. However, a clear

*sankarndf@gmail.com
†choisky99@skku.edu

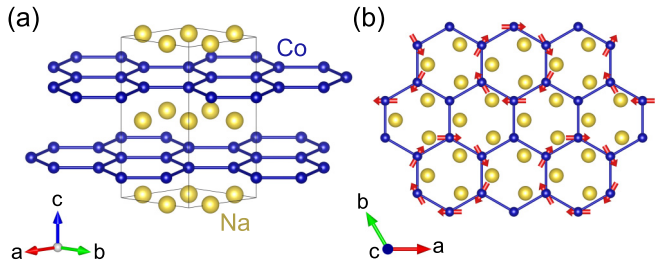

FIG. 1. (a) Crystal structure of $Na_2Co_2TeO_6$. The honeycomb layers consist of the coupled Co spins via the superexchange interaction Co-O-Co in the *ab* plane, which are separated by the NaO_6 triangular prisms. The solid blue lines connecting the Co atoms in the *ab* plane indicate the intra-honeycomb exchange coupling J. The O and Te atoms are omitted for clarity. (b) Sketch of a triple-**q** order of the Co spins, composed of the superposition of three zigzag order parameters [22]. The red arrows represent the spin alignments in the *ab* plane. The Co spins without the red arrows denote spinless sites.

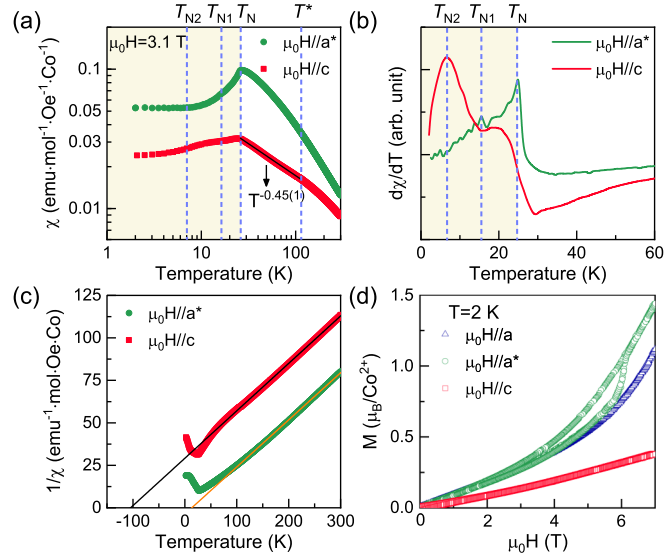

FIG. 2. (a) Temperature dependence of the dc magnetic susceptibility for $\mu_0 H \parallel a^*$ and $\mu_0 H \parallel c$ in a log-log scale. The shaded region represents the antiferromagnetically ordered state below T_N. The dashed lines denote the magnetic transition and crossover temperatures. The black solid line indicates the power-law behavior $\chi(T) \sim T^{-0.45(1)}$. (b) First derivative of the dc magnetic susceptibility $d\chi(T)/dT$. The peaks correspond to the magnetic transition and anomalies. (c) Inverse magnetic susceptibility $1/\chi(T)$ for each field direction. The solid lines are fits of the $1/\chi(T)$ data to the Curie-Weiss law. (d) Magnetization curves measured at 2 K for three different field directions.

landscape about static and dynamic magnetism is lacking in light of the purported generalized Kitaev honeycomb lattice model.

In this paper, we employ nuclear magnetic resonance (NMR) as a local probe to elucidate thermal evolution of magnetic orders and correlations of the Co^{2+} spins in $Na_2Co_2TeO_6$. ^{23}Na NMR spectral and relaxation measurements uncover multiple transitions and anisotropic spin dynamics, which are inexplicable within Heisenberg interaction. These results showcase the significant role of Kitaev and anisotropic exchange interactions in fine-tuning static and dynamic magnetism.

II. EXPERIMENTAL DETAILS

Polycrystalline samples of $Na_2Co_2TeO_6$ were prepared by a conventional solid-state reaction. The high-purity starting materials Na_2O, Co_3O_4, and TeO_2 were mixed in an appropriate stoichiometric molar ratio, and the mixture was ground thoroughly and sintered at 800 °C in air for 100 h in a Pt crucible. To obtain a single phase, the mixture was ground and sintered several times. Next, we grew high-quality single crystals of $Na_2Co_2TeO_6$ by the self-flux method. The mixture was ground thoroughly with the help of a mortar pestle, kept in a Pt crucible, and then gradually heated to 900 °C at 5 °C/min in air. The temperature of 900 °C was retained for 30 h, and then the sample was cooled to a temperature of 500 °C at the rate of 3 °C/h. On cooling down to room temperature, we obtained light-purple flaky crystals of $Na_2Co_2TeO_6$ with a typical size of 1–5 mm in diameter and 0.5 mm thick. The excessive flux was washed off with 100 °C water and 1*M* NaOH solution.

Static magnetic susceptibility and magnetization were measured using a VSM-SQUID magnetometer (MPMS3, Quantum Design). ^{23}Na ($I = 3/2$ and gyromagnetic ratio $\gamma_N = 11.262$ MHz/T) nuclear magnetic resonance (NMR) experiments were carried out using a MagRes spectrometer (developed at NHMFL, USA) with a 14 T Oxford Teslatron PT superconducting magnet. The temperature is varied between 2 and 300 K and a magnetic field is applied for the directions parallel and perpendicular to the Co^{2+} honeycomb layers. We used a silver coil because ^{23}Na (11.262 MHz/T) and ^{63}Cu (11.319 MHz/T) have a close gyromagnetic ratio. In the process of tracking all peaks, we varied a magnetic field for a fixed frequency $\nu = 35$ MHz and measured point by point with 0.01 T interval. The ^{23}Na NMR spectra were acquired by a standard Hahn echo method with a $\pi/2$ pulse length of $\tau_{\pi/2} = 10$ μs. The nuclear spin-lattice and spin-spin relaxation times T_1 and T_2 were measured with the saturation recovery and the Hahn echo technique, respectively, with single saturation pulse $\pi/2 - t - \pi/2 - \pi$ ($\tau_{\pi/2} = 2$–2.5 μs). The nuclear magnetization M versus elapsed time t was fitted to $1 - M(t)/M_\infty = A\{0.9\exp[-(6t/T_1)^\beta] + 0.1\exp[-(t/T_1)^\beta]\}$, where β is the stretching exponent and A is the fitting parameter. The relaxation rates differ between split peaks by less than 5%.

III. RESULTS AND DISCUSSION

A. Static magnetic susceptibility and magnetization

We present the temperature dependence of the static magnetic susceptibility $\chi(T)$ of $Na_2Co_2TeO_6$ in Fig. 2(a). $\chi(T)$ is larger for $\mu_0 H \parallel a^*$ than $\mu_0 H \parallel c$, suggesting the presence of substantial XY-type magnetic anisotropy. With decreasing temperature, $\chi(T)$ for both field directions shows an anomaly at $T_N = 26$ K, indicating long-range magnetic ordering. We mention that our $\chi(T)$ measurements were performed at a relatively high magnetic field of $\mu_0 H = 3.1$ T for

comparative purposes to the ^{23}Na NMR data. This may explain why our critical temperature $T_N = 26$ K is slightly lower than the reported transition temperature [19–21].

To identify magnetic transitions, we take a first derivative of $\chi(T)$ with respect to temperature [see Fig. 2(b)]. $d\chi/dT$ shows a sharp peak at T_N and a broad maximum at $T_{N2} = 7$ K for $\mu_0 H \parallel c$. Overall, the observed characteristic temperatures are comparable to the previous results [13,17,20,24,26]. However, the anomaly at $T_{N1} = 16$ K is less obvious for our sample. The salient feature is that $\chi(T)$ for $\mu_0 H \parallel c$ follows the power-law $T^{-0.45(1)}$ for the temperature range of $T_N < T < T^* = 115$ K. The anomalous power-law behavior highlights exotic magnetic correlations.

In Fig. 2(c), we plot the inverse magnetic susceptibility for both crystallographic axes. For the temperatures above T^*, the Curie-Weiss fits yield $\Theta^c_{CW} = -104.5(2)$ K and $\mu^c_{eff} = 5.35\ \mu_B$ for $\mu_0 H \parallel c$, and $\Theta^{a^*}_{CW} = 13.2(2)$ K and $\mu^{a^*}_{eff} = 5.37\ \mu_B$ for $\mu_0 H \parallel a^*$. The obtained parameters are in agreement with the previous studies [13,17,20,24,26]. The opposite sign of Θ_{CW} between the in-plane and the out-of-plane field directions is reminiscent of α-$RuCl_3$, pointing to the presence of various competing exchange interactions [28].

The isothermal magnetization curves $M(H)$ are shown in Fig. 2(d). For $\mu_0 H \parallel c$, $M(H)$ exhibits a linear increment up to 7 T, indicative of the predominant out-of-plane antiferromagnetic correlations. On the other hand, $M(H)$ for the a axis increases linearly and changes to a concave curvature above 4 T, while $M(H)$ for the a^* axis shows an apparent hysteric behavior near 6 T. The magnetic-field-direction dependent $M(H)$ supports the presence of XY-like magnetic anisotropy as well as magnetic anisotropy within the honeycomb layer. The observed first-order transition for $\mu_0 H \parallel a^* \approx 6$ T is associated with the field-induced reversal of moment canting, as discussed in the previous study [24].

B. ^{23}Na NMR spectra

Figure 3 presents the temperature-dependent ^{23}Na NMR spectra of $Na_2Co_2TeO_6$ in a stacked plot. The NMR signal amplitude was normalized to the maximum value. An external magnetic field is swept along the directions perpendicular or parallel to the ab honeycomb plane while fixing the RF frequency at $\nu = 35$ MHz. In the paramagnetic state above T_N, we observe a narrow single line with no quadrupole splitting for both orientations. On cooling below T_N, the NMR peak begins to split. For $\mu_0 H \parallel c$, the ^{23}Na NMR line splits into two peaks [designated as P_{1c} and P_{2c} in Fig. 3(a)] while for $\mu_0 H \parallel ab$, the line splits into four peaks P_{1p}, P_{2p}, P_{3p}, and P_{4p} as indicated in Fig. 3(b). This suggests that the Na site experiences the static internal field that relies strongly on the orientation, implying a complex magnetic structure.

We comment on the spin structure in the magnetically ordered state. The splitting of the NMR line with no appreciable broadening is a signature of a commensurate magnetic structure. In previous neutron scattering measurements [19–21,25–27], $Na_2Co_2TeO_6$ is widely accepted to have a zigzag AFM order. In the case of zigzag-type AFM order, we expect two split peaks in the NMR spectra. In this regard, the observed four in-plane components of the internal field at the Na site contradict the simple zigzag structure. In this situation, a very

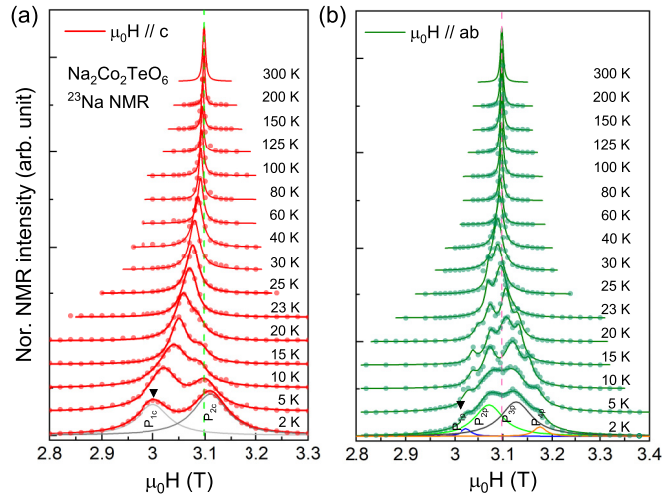

FIG. 3. Temperature dependence of the field-swept ^{23}Na NMR spectra (colored circles) of $Na_2Co_2TeO_6$ for a magnetic field applied to (a) perpendicular ($\mu_0 H \parallel c$) and (b) parallel ($\mu_0 H \parallel ab$) to a honeycomb layer. The solid lines represent the fitted theoretical curves and the vertical dashed lines are guides to the eye for the NMR line shift.

recent neutron study by Chen *et al.* [22] has come to our attention, showing that the magnetic ground state is described by a triple-**q** rather than zigzag structure. As sketched in Fig. 1(b), the triple-**q** magnetic structure is composed of the zigzag patterns and vortex spin texture with the spinless sites. The Co^{2+} moments have four or six in-plane components and AFM out-of-plane component. Accordingly, the NMR spectrum will be split into six or four lines. Within the extended Kitaev model, the off-diagonal symmetric Γ term is known to lead to spin canting toward the out-of-plane direction. On a qualitative level, the newly refined triple-**q** AFM order with the Néel-type canting along the c axis is compatible with the observed splitting to four lines for $\mu_0 H \parallel ab$ and two lines for $\mu_0 H \parallel c$. Nonetheless, a hyperfine coupling tensor should be determined to corroborate the triple-**q** magnetic structure with aid of angle-dependent NMR measurements.

In Fig. 4(a), we plot the temperature dependence of the relative NMR shift $K_m(T)$ on a semilogarithmic scale. $K_m(T)$ is defined by $K_m(\%) = [B_{ref} - B(T)]/B(T) \times 100\%$ with $B_{ref} = 2\pi\nu/\gamma_N$. We determined the resonance field $B(T)$ as a function of temperature by fitting the ^{23}Na NMR spectra to a single Gaussian function above T_N and multiple Gaussian profiles below T_N.

On cooling down to T_N, the peaks shift toward lower fields for both orientations. For temperatures above T_N, we observe the close resemblance between the magnetic susceptibility $\chi(\mu_0 H = 3.1\ \text{T})$ and $K_m(T)$ [see the blue line in the upper panel of Fig. 4(a)]. Using the Clogston-Jaccarino $K_m - \chi$ plot, we estimate the hyperfine interaction A_{hf} between the ^{23}Na nuclear spins and the Co^{2+} electron spins. As shown in the inset of Fig. 4(a), $A^c_{hf} = 30 \pm 1.5\ \text{mT}/\mu_B$ in the $T = 60$–300 K temperature range is increased to $A^c_{hf} = 80 \pm 0.2\ \text{mT}/\mu_B$ at $T = 30$–60 K. The enhanced A^c_{hf} at low temperatures is ascribed to the additional contribution of the short-range ordered Co^{2+} spins to the hyperfine coupling

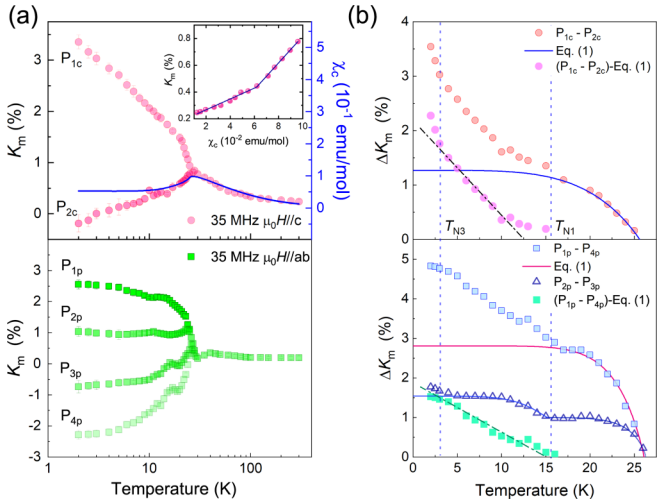

FIG. 4. (a) Semilog plot of the magnetic shift $K_m(T)$ vs T of the ^{23}Na nuclear spins measured in the field directions of $\mu_0H \parallel c$ (pink circles) and $\mu_0H \parallel ab$ (green squares). The blue solid line is the temperature dependence of static magnetic susceptibility $\chi_c(T)$. The inset plots $K_m(T)$ vs χ_c. The solid line is the fit to the Clogston-Jaccarino relation. (b) Temperature dependence of the peak difference ΔK_m between the two split peaks for $\mu_0H \parallel c$ (pink circles) and $\mu_0H \parallel ab$ (azure squares). The solid lines are the theoretical curves fitted to Eq. (1) as described in the main text. The pink and green symbols represent the residual ΔK_m obtained by subtracting Eq. (1) from $K_m(T)$. The dot-dashed linear lines are guides to the eye. The vertical dashed lines indicate the magnetic anomalies at $T_{N3} = 3.5$ K and $T_{N1} = 16$ K in the magnetically ordered state.

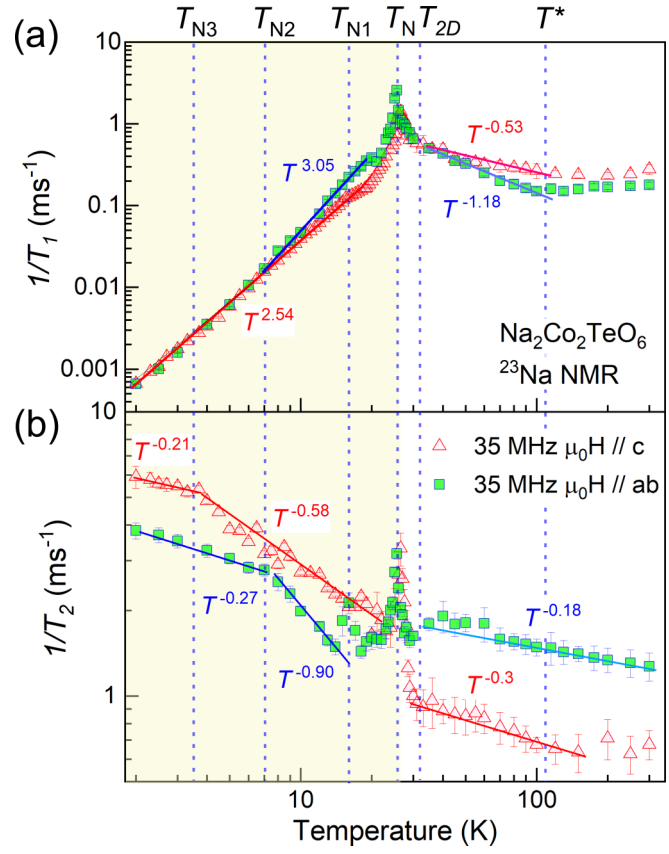

FIG. 5. (a) Spin-lattice relaxation rate $1/T_1$ and (b) spin-spin relaxation rate $1/T_2$ plotted as a function of temperature on a double logarithmic scale. The straight lines are power-law fits at the selected temperature intervals. The vertical lines denote the characteristic and transition temperatures at $T_{N3} = 3.5$, $T_{N2} = 7$, $T_{N1} = 16$, $T_N = 26$, $T_{2D} = 32$, and $T^* = 110$ K.

constant because there is no evidence of a structural transition or anomaly.

Below T_N, we observe the line splitting, which is caused by the development of the Co^{2+} sublattice magnetization. This is what is expected for a long-range magnetic order. To trace the temperature evolution of the staggered magnetization, we plot the T dependence of $\Delta K_m(T)$, which is proportional to the field difference between the two split peaks. As shown in Fig. 4(b), $\Delta K_m(T)$ first shows an order-parameter-like increase with decreasing temperature below T_N. This is described by the phenomenological expression

$$\Delta K_m(T) = \Delta K_m(T = 0\ \mathrm{K})[1 - (T/T_N)^{\delta}]^{\beta}, \qquad (1)$$

where $\delta \approx 2.2$–9.1 and $\beta \approx 0.62$ (depending on the peak separation) are the phenomenological parameters. Due to the scarce data points near T_N, extracting the critical exponent of the order parameter is subject to uncertainties. Nonetheless, we find that the β value is comparable to the critical exponent $\alpha = 0.58(9)$ determined from the $1/T_1$ (see below).

The fitting analysis allows identifying the two magnetic anomalies in the ordered state. Apparently, the theoretical curves (solid lines) deviate from $\Delta K_m(T)$ at $T_{N1} = 16$ K. In lieu of saturation, we observe a continuous linear increase for the peak separation between P_{1c} and P_{2c} and between P_{1p} and P_{4p} or another order-parameter-like increase for the peak separation between P_{2p} and P_{3p}. To articulate this anomaly, we subtract the raw $\Delta K_m(T)$ from the fitted theoretical curves. The resulting data [pink circles and green squares in Fig. 4(b)] show a linear increase with a small but discernible anomaly at $T_{N3} = 3.5$ K. We recall that similar anomalies of the magnetic order parameters have been reported in the anisotropic spin tetramer system $CdCu_2(BO_3)_2$ with four inequivalent exchange couplings and the staircase kagome lattice compound $PbCu_3TeO_7$ [29,30]. This anomaly is ascribed to a reorientation of the spins resulting from the competing exchange interactions. We further note that the neutron and thermodynamic measurements uncover a subtle change in the magnetic structure at 18 K [13,22,24], corresponding to $T_{N1} = 16$ K. This lends support to the interpretation of spin rearrangements.

C. ^{23}Na nuclear relaxation rates

To probe the Co^{2+}-ion spin dynamics sensed at the Na nuclei, we investigated the ^{23}Na nuclear spin-lattice and spin-spin relaxation rates ($1/T_1$ and $1/T_2$) across the successive magnetic phase transitions. The relaxation measurements were performed on the leftmost peaks denoted by the downward triangles in Fig. 3. Shown in Fig. 5 are log-log plots of $1/T_1$ and $1/T_2$ versus T. Our in-plane (green squares) and out-of-plane (pink triangles) results unveil the multistage T development of magnetic correlations as inferred from

distinctly changing power-law behaviors (straight lines) of both $1/T_1$ and $1/T_2$.

We first discuss spin dynamics in the paramagnetic ($T > T_N$) state. On cooling down through $T^* \approx 110$ K, $1/T_1$ starts to develop a power-law increase: $1/T_1 \sim T^n$ with $n = -1.18$ for $\mu_0 H \parallel ab$ and $n = -0.53$ for $\mu_0 H \parallel c$. The onset of the power law $1/T_1$ is an indication that a quickly fluctuating paramagnetic regime, featuring the T-independent $1/T_1$ behavior, transits to a correlated paramagnetic state. Noticeably, the crossover T^* from a trivial to a correlated paramagnet occurs near the out-of-plane Weiss temperature $\Theta^c_{CW} = -104.5(2)$ K. We further note that the out-of-plane $\chi_c(T)$ shows the power-law increase $T^{-0.45(1)}$ in the same temperature range [see the solid line in Fig. 2(a)]. The development of short-range magnetic correlations at the temperature scale of Θ is a hallmark of low-dimensional or frustrated magnets. Further, the larger exponent n of the in-plane $1/T_1^{ab}$ than the out-of-plane $1/T_1^c$ implies the predominance of quasi-two-dimensional transverse spin correlations. As the temperature approaches the transition temperature, $1/T_1$ ceases to follow the power-law dependence at $T_{2D} = 32$ K and exhibits a sharp peak at $T_N = 26$ K, consistent with our $\chi(T)$ result. A divergent $1/T_1$ due to critical slowing down of spin fluctuations is a fingerprint of long-range magnetic ordering. We stress that the T_{2D} temperature corresponds to a 2D magnetic order at 31.0 K observed by a recent zero-field neutron diffraction study [22].

Before proceeding, we recall that $1/T_1$ is dictated by the transverse fluctuations of the local field at the ^{23}Na nuclear site with respect to the external field. On the other hand, $1/T_2$ probes spin dynamics caused by the longitudinal and transverse fluctuations of the local field, which conserves nuclear spin reservoir energy. Similarly to $1/T_1$, $1/T_2$ also follows a power-law dependence in the wide paramagnetic state down to $T_{2D} = 32$ K: $1/T_2 \sim T^{-0.18}$ for $\mu_0 H \parallel ab$ and $T^{-0.30}$ for $\mu_0 H \parallel c$. In addition, $1/T_2$ shows a sharp peak at T_N for both directions. The salient feature is that $1/T_1$ and $1/T_2$ exhibit a disparate power-law dependence in their temperature and orientation. More specifically, the out-of-plane $1/T_2$ displays a stronger T dependence than the in-plane $1/T_2$, which is converse to $1/T_1$. The anisotropic spin-spin correlations are supported by the static magnetic susceptibility, in which only the out-of-plane $\chi_c(T)$ displays a power-law behavior. Taken together, the correlated paramagnetic state entails anisotropic spin dynamics, which is incompatible with a Heisenberg-type spin system. Rather, Kitaev or symmetric anisotropic Γ exchange interactions may be evoked as a control parameter of spin-spin correlations.

To shed light on the nature of the correlated paramagnetic state, we further analyze the temporal development of magnetic correlations in terms of the nonlinear σ model for 2D frustrated antiferromagnets [31–34]. In this model, the magnetic correlation length is given by $\xi \propto \exp(4\pi\rho_S/T)/\sqrt{T}$ with a spin stiffness constant ρ_S and the nuclear spin-lattice relaxation rate is $1/(T_1T^3) \propto \exp(4\pi\rho_S/T)$.

In view of examining the validity of this model, we present semilog plot $1/(T_1T^3)$ vs $100/T$ for $\mu_0 H \parallel c$ (pink triangles) and $\mu_0 H \parallel ab$ (azure squares) in Fig. 6. The dashed lines are the extrapolation of the constant $1/(T_{1\infty}T^3)$ value to low temperatures. $T_{1\infty} = 5.57$ ms is evaluated at $T = 300$ K (corresponding to an exchange-narrowing limit). We find that

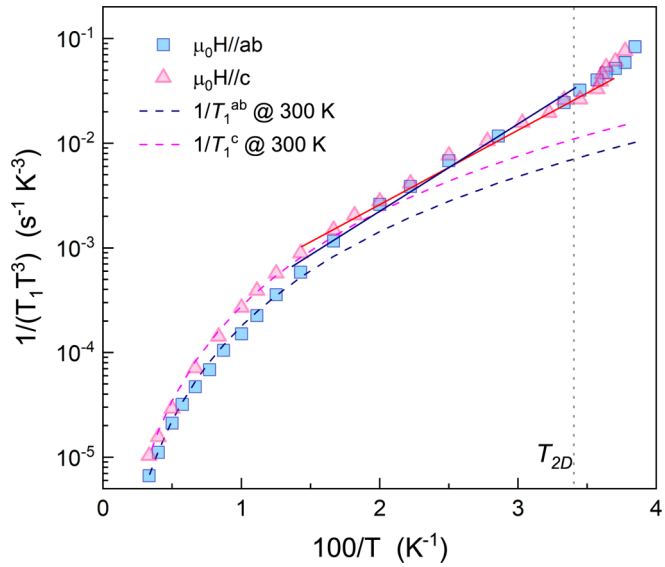

FIG. 6. Semilog plot of $1/(T_1T^3)$ vs $100/T$ for $\mu_0 H \parallel c$ (pink triangles) and $\mu_0 H \parallel ab$ (azure squares). The dashed lines are the low-T extrapolation of $1/(T_1T^3)$ evaluated in the simple paramagnetic limit at $T = 300$ K. The solid lines are fits to $1/(T_1T^3) \propto \exp(4\pi\rho_S/T)$ as described in the main text. The vertical dotted line marks the characteristic temperature $T_{2D} = 32$ K.

the nonlinear σ model gives a nice description of $1/(T_1T^3)$ in the temperature between T_{2D} and ≈ 70 K (see the solid lines in Fig. 6). The obtained values of $4\pi\rho_S \approx 69$–77 K are somewhat smaller than the Weiss temperature $\Theta^c_{CW} = -104.5(2)$ K. This suggests that the spin-spin correlations of $Na_2Co_2TeO_6$ in the correlated paramagnetic state are largely captured by the 2D renormalized classical behavior.

We next turn to the magnetically ordered state ($T < T_N$), in which the $1/T_1$ relaxation mechanism is dictated by a distinct channel from the high-T paramagnetic state. The scattering of magnons off nuclear spins is mainly responsible for $1/T_1$. For $\mu_0 H \parallel c$, $1/T_1$ obeys a power-law dependence $1/T_1 \sim T^{2.54}$ in the temperature range between $T = 2$ K and $T_{N1} = 16$ K. On the other hand, we observe the slight change of the exponent at $T_{N2} = 7$ K for $\mu_0 H \parallel ab$: $1/T_1 \sim T^{2.54}$ for $T < T_{N2}$ and $T^{3.05}$ for $T_{N2} < T < 20$ K. The static $\chi(T)$ exhibits the same field-orientation dependence of the magnetic anomalies as the local dynamic probe; the in-plane (out-of-plane) $\chi(T)$ is selectively sensitive to T_{N1} (T_{N2}), as seen in Fig. 2(b). Considering the observed T dependence of $1/T_1$ is close to a T^3 behavior, the relaxation process is mainly governed by a two-magnon Raman mechanism. Nonetheless, the somewhat weaker dependence than T^3 may indicate coexistence of 3D and 2D spin waves, inferred from the neutron diffraction result that alludes to the coexisting 3D and 2D magnetic orders [22].

Unlike the T^3-like decrease in $1/T_1$, $1/T_2$ continues to increase as the temperature is lowered below T_{N1} showing a wipe-out effect. The largely contrasting behavior between the $1/T_1$ and $1/T_2$ means that the $1/T_1$ contribution to $1/T_2$ is negligible and that slow spin dynamics is present in the ordered state. This suggests that the Co^{2+} magnetic moments are not frozen despite their spin ordering. Below T_N, we observe a weak yet discernible peak at T_{N1} only for $\mu_0 H \parallel ab$,

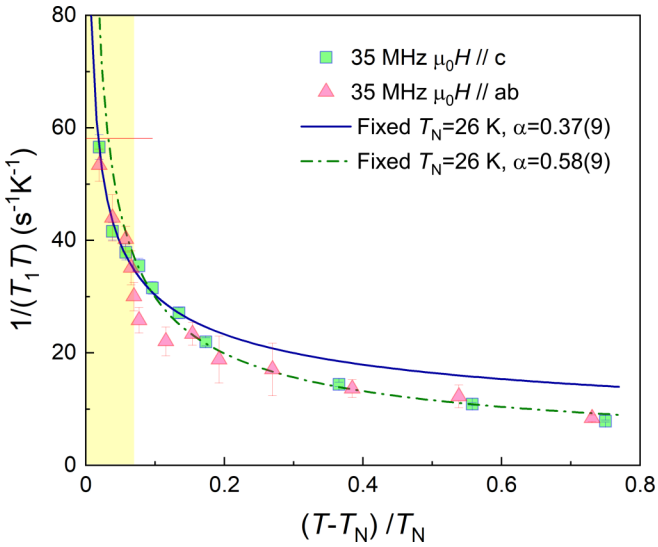

FIG. 7. $1/(T_1T)$ vs $(T - T_N)/T_N$. The solid and the dash-dotted lines are fits to the relation $1/(T_1T) \propto (T/T_N - 1)^{\alpha}$.

indicating that the spin orientation is dominantly driven by in-plane magnetic correlations. For temperatures below T_{N1}, $1/T_2$ displays a power-law-like increase with an orientation-dependent change of its slope. For $\mu_0H \parallel c$, $1/T_2$ changes the exponent from $n = -0.56$ to -0.21 with decreasing temperature through $T_{N3} = 3.5$ K. However, for $\mu_0H \parallel ab$, the exponent is varied from $n = -0.90$ to -0.27 through T_{N2}, at which $1/T_1$ shows the exponent change. By the same token as in the paramagnetic state, the distinct orientation dependence of $1/T_2$ suggests an anisotropic development of magnetic correlations between the intra- and interhoneycomb layers.

In Heisenberg-type antiferromagnets, interlayer interactions set the 3D magnetic ordering. In the presence of frustration, 2D magnetic correlations can survive in the 3D ordered state. However, it is impossible to comprehend the successive power-law-like dependence, the anisotropic behaviors of $1/T_1$, and $1/T_2$ and the 2D magnetic order at T_{2D}. Given that the four magnetic anomalies and transitions are identified in the ordered state, a minimal spin Hamiltonian may contain more than five magnetic parameters. Indeed, recent neutron data were discussed in terms of a J_1-J_3-K-Γ-Γ' model [25–27]. This Hamiltonian contains two types of exchange frustration, namely, J_1-J_3-type frustration and Kitaev-type frustration. On a qualitative level, this together with an energy hierarchy of these competing, anisotropic exchange interactions can engender a successive change or modulation of the ordered spin orientation. In addition, an order-disorder crossover in the vortex spin texture or the swinging or vibration patterns of a triple-**q** structure provide the possibility of bringing about rich low-energy spin dynamics.

Lastly, the divergence of $1/T_1$ is a signature of a second-order magnetic phase transition. For a quantitative analysis of critical phenomena, $1/(T_1T)$ versus $(T - T_N)/T_N$ is plotted in Fig. 7 and is fitted to the relation $1/(T_1T) \propto (T/T_N - 1)^{\alpha}$ with the critical exponent α. In the vicinity of the phase transition, $(T - T_N)/T_N < 0.1$, we obtain $\alpha \approx 0.37(9)$ (blue solid line in Fig. 7) by fixing the transition temperature to $T_N = 26$ K. We further find the critical exponent $\alpha \approx 0.58(9)$ (green dash-dotted line) in the wide temperature range of $T > T_{2D}$. This value is larger than $\alpha = 0.5$ predicted by a mean-field theory of a 3D isotropic Heisenberg antiferromagnet [35]. The changing critical exponent through T_{2D} provides indirect support that the 3D critical regime $(T - T_N)/T_N < 0.1$ is narrowed by the 2D renormalized classical regime.

IV. CONCLUSIONS

In conclusion, we have presented combined static magnetic susceptibility and ^{23}Na NMR measurements of $Na_2Co_2TeO_6$. In a high-temperature paramagnetic state, $1/T_1$ and $1/T_2$ as well as a static magnetic susceptibility feature a power-law behavior for temperatures below $T^* \approx 110$ K, depending on an external field direction. We find that these anisotropic spin-spin correlations are described by a 2D renormalized classical behavior. We further identify the precursor transition at $T_{2D} = 32$ K, which separates the 2D renormalized classical behavior from the narrow 3D critical regime ($T_N < T < T_{2D}$). In a magnetically ordered state, the ^{23}Na NMR and $\chi(T)$ data disclose the occurrence of three successive magnetic anomalies in addition to the 3D long-range order at T_N. The multiple transitions and crossovers are anisotropic with respect to an applied field direction, indicating an energy hierarchy of competing, anisotropic exchange interactions. Our NMR results are not typical for a pristine Kitaev model, casting doubts on the notion that the Kitaev interaction is a leading term. More theoretical and experimental work will be needed to model the effective spin Hamiltonian of $Na_2Co_2TeO_6$.

ACKNOWLEDGMENTS

K.-Y.C. was supported by the National Research Foundation (NRF) of Korea (Grants No. 2020R1A2C3012367 and No. 2020R1A5A1016518). R.S. acknowledges financial support provided by the Ministry of Science and Technology in Taiwan under Projects No. MOST-108-2112-M-001-049-MY2 and No. MOST 109-2124-M-002-001.

[1] A. Kitaev, Ann. Phys. **321**, 2 (2006).
[2] S. M. Winter, A. A. Tsirlin, M. Daghofer, J. van den Brink, Y. Singh, P. Gegenwart, and R. Valent, J. Phys.: Condens. Matter **29**, 493002 (2017).
[3] M. Hermanns, I. Kimchi, and J. Knolle, Annu. Rev. Condens. Matter Phys. **9**, 17 (2018).
[4] H. Takagi, T. Takayama, G. Jackeli, G. Khaliullin, and S. E. Nagler, Nat. Rev. Phys. **1**, 264 (2019).
[5] G. Jackeli and G. Khaliullin, Phys. Rev. Lett. **102**, 017205 (2009).
[6] S. K. Choi, R. Coldea, A. N. Kolmogorov, T. Lancaster, I. I. Mazin, S. J. Blundell, P. G. Radaelli, Y. Singh, P. Gegenwart,

K. R. Choi, S.-W. Cheong, P. J. Baker, C. Stock, and J. Taylor, Phys. Rev. Lett. **108**, 127204 (2012).

[7] K. W. Plumb, J. P. Clancy, L. J. Sandilands, V. V. Shankar, Y. F. Hu, K. S. Burch, H.-Y. Kee, and Y.-J. Kim, Phys. Rev. B **90**, 041112(R) (2014).

[8] S.-H. Do, S.-Y. Park, J. Yoshitake, J. Nasu, Y. Motome, Y. S. Kwon, D. T. Adroja, D. J. Voneshen, K. Kim, T.-H. Jang, J.-H. Park, K.-Y. Choi, and S. Ji, Nat. Phys. **13**, 1079 (2017).

[9] H. Liu and G. Khaliullin, Phys. Rev. B **97**, 014407 (2018).

[10] R. Sano, Y. Kato, and Y. Motome, Phys. Rev. B **97**, 014408 (2018).

[11] H. Liu, J. Chaloupka, and G. Khaliullin, Phys. Rev. Lett. **125**, 047201 (2020).

[12] Y. Motome, R. Sano, S. Jang, Y. Sugita, and Y. Kato, J. Phys.: Condens. Matter **32**, 404001 (2020)

[13] L. Viciu, Q. Huang, E. Morosan, H. Zandbergen, N. Greenbaum, T. McQueen, and R. Cava, J. Solid State Chem. **180**, 1060 (2007).

[14] C. Wong, M. Avdeev, and C. Ling, J. Solid State Chem. **243**, 18 (2016).

[15] H. K. Vivanco, B. A. Trump, C. M. Brown, and T. M. McQueen, Phys. Rev. B **102**, 224411 (2020).

[16] J.-Q. Yan, S. Okamoto, Y. Wu, Q. Zheng, H. D. Zhou, H. B. Cao, and M. A. McGuire, Phys. Rev. Materials **3**, 074405 (2019).

[17] G. Xiao, Z. Xia, W. Zhang, X. Yue, S. Huang, X. Zhang, F. Yang, Y. Song, M. Wei, H. Deng, and D. Jiang, Cryst. Growth Des. **19**, 2568 (2019).

[18] R. Zhong, T. Gao, N. P. Ong, and R. J. Cava, Sci. Adv. **6**, eaay6953 (2020).

[19] E. Lefranois, M. Songvilay, J. Robert, G. Nataf, E. Jordan, L. Chaix, C. V. Colin, P. Lejay, A. Hadj-Azzem, R. Ballou, and V. Simonet, Phys. Rev. B **94**, 214416 (2016).

[20] A. K. Bera, S. M. Yusuf, A. Kumar, and C. Ritter, Phys. Rev. B **95**, 094424 (2017).

[21] Y. Mao and Y. Li, Phys. Rev. B **102**, 054414 (2020).

[22] W. Chen, X. Li, Z. Hu, Z. Hu, L. Yue, R. Sutarto, F. He, K. Iida, K. Kamazawa, W. Yu, X. Lin, and Y. Li, Phys. Rev. B **103**, L180404 (2021).

[23] R. Berthelot, W. Schmidt, A. Sleight, and M. Subramanian, J. Solid State Chem. **196**, 225 (2012).

[24] W. Yao and Y. Li, Phys. Rev. B **101**, 085120 (2020).

[25] M. Songvilay, J. Robert, S. Petit, J. A. Rodriguez-Rivera, W. D. Ratcliff, F. Damay, V. Baledent, M. Jimenez-Ruiz, P. Lejay, E. Pachoud, A. Hadj-Azzem, V. Simonet, and C. Stock, Phys. Rev. B **102**, 224429 (2020).

[26] G. Lin, J. Jeong, C. Kim, Y. Wang, Q. Huang, T. Masuda, S. Asai, S. Itoh, G. Güunther, M. Russina, Z. Lu, J. Sheng, L. Wang, J. Wang, G. Wang, Q. Ren, C. Xi, W. Tong, L. Ling, Z. Liu, *et al.*, arXiv:2012.00940.

[27] C. Kim, J. Jeong, G. Lin, P. Park, T. Masuda, S. Asai, S. Itoh, H.-S. Kim, H. Zhou, J. Ma, and J.-G. Park, arXiv:2012.06167.

[28] S.-H. Do, W.-J. Lee, S. Lee, Y. S. Choi, K.-J. Lee, D. I. Gorbunov, J. Wosnitza, B. J. Suh, and K.-Y. Choi, Phys. Rev. B **98**, 014407 (2018).

[29] W.-J. Lee, S.-H. Do, Sungwon Yoon, Z. H. Jang, B. J. Suh, J. H. Lee, A. P. Reyes, P. L. Kuhns, H. Luetkens, and K.-Y. Choi, Phys. Rev. B **90**, 214416 (2014).

[30] S. W. Yoon, C. H. Lee, S. Lee, Y. S. Choi, S.-H. Do, M. Abdel-Jawad, I. Watanabe, B. J. Suh, and K.-Y. Choi, Phys. Rev. B **98**, 214401 (2018).

[31] P. Azaria, B. Delamotte, and D. Mouhanna, Phys. Rev. Lett. **68**, 1762 (1992).

[32] A. V. Chubukov, T. Senthil, and S. Sachdev, Phys. Rev. Lett. **72**, 2089 (1994).

[33] A. V. Chubukov, S. Sachdev, and T. Senthil, Nucl. Phys. B **426**, 601 (1994).

[34] Y. Itoh, JPS Conf. Proc. **3**, 014006 (2014).

[35] T. Moriya and K. Ueda, Solid State Commun. **15**, 169 (1974).